

Intragranular Fracture Mechanism of Highly Crystalline Lithium Manganese Oxide during Lithium Insertion/Extraction Reactions

Kingo Ariyoshi, Nan Ukumori

Citation	ACS Applied Energy Materials. 4(8); 8142-8149
Issue Date	2021-07-28
Type	Journal Article
Textversion	Author
Supporting Information	<p>The Supporting Information is available free of charge at https://pubs.acs.org/doi/10.1021/acsaem.1c01442.</p> <p>Schematic illustrations of internal stresses generated in lithium insertion materials; XRD patterns of LMO electrodes during charge and discharge; SEM images of LMO particles after the accelerated cycle test; particle fracture of Li[Li_{0.1}Mn_{1.9}]O₄; SEM images of LMO particles after the overcharge test; SEM images of LMO particles after the cycle test in the 3 V region; and XRD patterns of LMO electrodes during discharge (PDF)</p>
Rights	<p>This document is the Accepted Manuscript version of a Published Work that appeared in final form in ACS Applied Energy Materials, copyright © AmericanChemical Society after peer review and technical editing by the publisher. To access the final edited and published work see https://doi.org/10.1021/acsaem.1c01442.</p>
DOI	10.1021/acsaem.1c01442

Self-Archiving by Author(s)
Placed on: Osaka City University

Intragranular Fracture Mechanism of Highly Crystalline Lithium Manganese Oxide (LiMn_2O_4) during Lithium Insertion/Extraction Reactions

Kingo Ariyoshi and Nan Ukumori*

Department of Applied Chemistry and Bioengineering, Graduate School of Engineering, Osaka City University, 3-3-138 Sugimoto, Sumiyoshi-ku, Osaka 558-8585, Japan.

ABSTRACT: Lithium-ion batteries require long cycle lives for efficient automobile and stationary applications. Therefore, the lithium-insertion materials used as positive and negative electrodes in batteries need to be highly durable. Lithium-insertion materials normally change their lattice dimensions during charge and discharge; therefore, particle fracture leading to the deterioration of the materials is one of the greatest hindrances to extending the cycle life. Despite its importance, no one has experimentally elucidated the fracture mechanism in detail. To avoid or suppress particle fracture, it is required to understand the fracture mechanisms, with an emphasis on the relationship between the change in lattice dimensions and the generation/propagation of cracks on the particles. In this study, we examined particle fracture phenomena using single-crystal LiMn_2O_4 (LMO) having an octahedral shape with a crystal size of $\sim 5 \mu\text{m}$. Accelerated cycle tests and overcharge tests revealed that during the lithium extraction reaction of LMO in the 4 V region, cracks are induced along the $\{111\}$ fracture planes by stress corrosion cracking, wherein the acid

generated by the decomposition of the electrolyte accelerates the crack propagation. During the lithium-insertion reaction of LMO in the 3 V region, wherein the structural transformation between the cubic and tetragonal lattices takes place, heavy cracks are caused by strong internal stresses at grain boundaries, {100} fracture planes at the cubic/tetragonal grain boundary, and {110} fracture planes at the tetragonal/tetragonal grain boundary. The results obtained herein suggest that crack patterns are closely related to the change in lattice dimensions for lithium-insertion materials. These findings provide useful insights into the development of lithium-insertion materials having excellent cyclability by designing particle morphology and size.

Keywords; Lithium-ion battery, Lithium manganese oxide, Highly-crystalline material, Particle fracture, Intragranular cracking, Stress corrosion cracking.

1. Introduction

In recent years, long-life lithium-ion batteries (LIBs) have become crucial for automobile and stationary applications, which require a long lifetime (cycle life and calendar life) of at least 10 years.¹⁻³ Since the lithium-insertion materials used as positive and negative electrodes in LIBs are the principal determinants of battery performance, excellent cyclability ensuring that the capacity does not fade even after 10000 cycles is required for designing long-lived LIBs. The most critical problem hindering long-term cyclability is the deterioration of materials due to the destruction of the crystal structure, dissolution of transition metals, formation of a high resistance interphase on the particle surface, and particle fracture, among other factors.⁴⁻⁶ In previous studies,⁷⁻¹³ highly crystalline LiMn_2O_4 -based materials exhibited superior cyclability to nano-sized materials having low crystallinity. The superior cyclability of highly crystalline materials stems from the greater

durability of the particle surface against the dissolution of materials and the decomposition of the electrolyte. Despite these advantages, the concern remains that the deterioration caused by particle fracture will occur for large, highly crystalline micro-scale particles, because a larger particle has a greater number of defects in the crystal, which promotes particle fracture.

As the development of lithium-insertion materials with long cycle lives is crucial, material degradation due to particle fracture has received much attention.¹⁴⁻¹⁷ The lattice dimensions of lithium-insertion materials change during charge and discharge; consequently, internal stress is generated due to dimensional mismatch, which causes particle fracture.¹⁸⁻²¹ The particle fracture leads to a disruption of the electron-conduction pathways, causing a decrease in capacity due to the loss of electrochemical contact between the particles.²²⁻²⁴ During the past two decades, extensive studies have been performed to understand the origin of particle fracture in relation to the change in the lattice dimensions of materials by means of acoustic emission histometry,²⁵⁻²⁸ dilatometry,²⁹⁻³² stress evolution measurements,³³⁻³⁶ and direct observation using electron microscopy.³⁷⁻⁴⁸ In addition to experimental studies, many computational approaches have been employed to understand fracture phenomena based on fracture mechanics.⁴⁹⁻⁶¹

Despite the experimental and computational attempts to understand particle fracture in lithium-insertion materials, the relationship between particle fracture and lithium-insertion mechanism remains unclear. Li insertion reactions are classified into homogeneous phase reactions and two-phase coexistence reactions, and the mechanism of stress generation inside the particle due to dimensional mismatch is also different between the two mechanisms (Fig. S1). For the single-phase reaction, the concentration gradient in the particle results in a continuous dimensional change in the particle, because the lattice dimension depends on the amount of Li ions in the structure. Conversely, for a two-phase reaction, a large dimensional mismatch occurs at the grain

boundary. Consequently, the internal stress for the two-phase reaction is expected to be larger than that for the single-phase reaction. In addition, the change in lattice dimension accompanying an insertion reaction has some variety: an isotropic change versus an anisotropic change consisting of a mixture of elongation and shrinkage along different lattice axes. To suppress particle fracture and establish design guidelines for long-lived materials, it is crucial to clarify the relationship between such structural changes and particle fracture from a crystallographic perspective. For example, along which crystal plane (crystal orientation) the crack is generated, how the orientation of the crack corresponds to the structural change, and how a crack forms and propagates of a crack are based on fracture mechanics.

In this study, the relationship between the lithium-insertion reaction mechanism and particle fracture mechanism was investigated for LiMn_2O_4 (LMO) using two different reaction mechanisms having different insertion schemes:⁶² a single-phase reaction versus a two-phase reaction, isotropic structural change versus anisotropic structural change. To clearly observe the particle fracture phenomenon, highly crystalline large-sized octahedral LMO particles $\sim 5 \mu\text{m}$ in size were used. By observing the fracture of highly crystallized LMO particles under severe conditions such as constant-voltage charge–discharge and overcharge tests, the mechanism of fracturing of lithium-insertion materials during charge–discharge is discussed from a crystallographic perspective.

2. Experimental Section

Lithium manganese oxides were prepared using a solid-state reaction. Stoichiometric LiMn_2O_4 was prepared from Li_2CO_3 and Mn_3O_4 in a one-to-two ratio of lithium and manganese. The reaction mixture was heated in air at $950 \text{ }^\circ\text{C}$ for 10 h, following which, the temperature was

decreased to 700 °C and maintained thereat for 20 h. $\text{Li}[\text{Li}_{1/3}\text{Ti}_{5/3}]\text{O}_4$ (LTO),⁶³ used as a negative electrode material, were obtained from Ishihara Sangyo Kaisha, Ltd., Japan (LTO; LT855-17C lot. 0042).

The particle morphologies of the samples were observed using scanning electron microscopy (SEM, VE-7800, Keyence Co. Ltd., Japan). The samples were placed on a conductive adhesive tape. The acceleration voltage was 8 kV. The particles contained in the electrode following the cycle tests were also observed using SEM. Following the cycle tests, the cells were opened in a glove box, and the positive electrode was washed using dimethyl carbonate (DMC) to remove the electrolyte. SEM was performed on the surface at the center of the electrode. Typical images collected from a few hundred sample particles are shown in the figures.

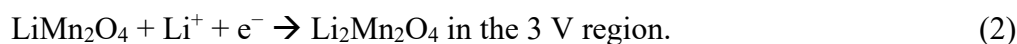
To prepare the LMO electrodes, acetylene black (AB) and polyvinylidene fluoride (PVdF) were mixed with LMO powder in an LMO:AB:PVdF ratio of 88:6:6. The mixture was diluted using N-methyl-2-pyrrolidone (NMP) to obtain a slurry. This slurry was cast onto a piece of aluminum foil (loading weight of approximately 24 mg cm²). Following heating at 140 °C overnight in a vacuum to volatilize NMP, the LMO electrode was punched into disks of 2 cm² area (1.6 cm diameter). The resulting LMO electrodes were tested in electrochemical cells (Type TJ-AC, Tomcell, Japan) consisting of a separator and lithium metal or LTO electrodes. The electrolyte used was 1 M LiPF_6 dissolved in ethylene carbonate (EC) and dimethyl carbonate (DMC) in an EC:DMC ratio of 3:7 by volume (Kishida Chemical Co. Ltd., Japan). All cells were assembled in an Ar-filled glove box.

3. Results and Discussion

3.1. Internal stress caused by dimensional mismatch in LMO particles during lithium insertion/extraction reaction

The structural and electrochemical properties of the synthesized LMO were characterized using X-ray diffraction (XRD), SEM and electrochemical measurements. From the XRD pattern (Fig. 1 a), all diffraction lines can be indexed by considering a cubic lattice. The XRD pattern was identical to that of the spinel structure, indicating that Li ions are located at the tetrahedral sites and Mn ions at the octahedral sites in the cubic-close-packed oxygen array. The cubic lattice parameter of LMO (8.24 Å) agrees well with the reported value.⁶² The particle morphology of LMO was observed using SEM (Fig. 1 b). Since LMO was prepared at a high temperature, the particles grew in an octahedron surrounded by smooth {111} facets. This indicates that the LMO surface was enclosed by an oxygen close-packed plane. Highly crystalline particles having large sizes and smooth facets are advantageous for monitoring particle fracture during a reaction. In addition, the particles were single crystals, lacking grain boundaries. Therefore, only single-particle fracture (intragranular fracture) occurs in these particles, which allows the investigation of the fracture mechanism in relation to structural changes.

Lithium insertion/extraction reactions of LMO proceed along two pathways, expressed in Equations 1 and 2:⁶²



During the reactions, the cubic lattice of LMO undergoes isotropic or anisotropic dimensional changes (Fig. 1 c). During lithium extraction from LMO (Eq. 1), the cubic lattice parameter decreased to 8.04 Å, corresponding to 2% isotropic contraction. During lithium insertion into the LMO (Eq. 2), cubic lattice changes to a tetragonal lattice with lattice parameters of $a_T = 8.00$ Å and $c_T = 9.25$ Å, resulting in the anisotropic distortion of the cubic lattice, 3% contraction along the a_T -axis and 12% expansion along the c_T -axis. The lithium-insertion reaction proceeded in two phases. These dimensional changes cause internal stresses in the particles which fracture them. As described earlier, lithium insertion/extraction proceeds in LMO proceeds via different two-phase and single-phase reaction mechanisms in the 3 V and 4 V regions, respectively (anisotropic versus isotropic structural change), which allows us to elucidate the relationship between the fracture mechanism and the lithium insertion mechanism.

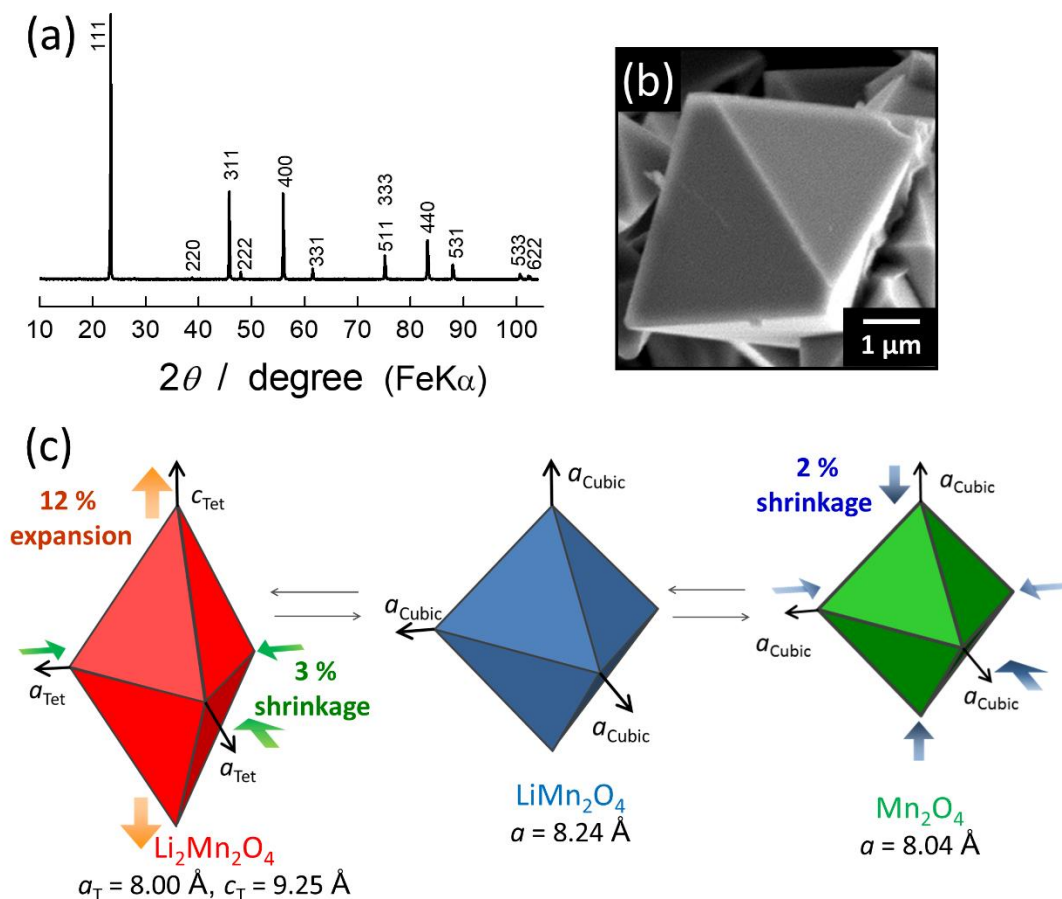


Figure 1. (a) XRD pattern and (b) SEM image of LMO. The morphology of LMO particles consists of a large octahedral single-crystal having smooth (111)-facets. (c) Change in lattice dimension of LMO during lithium insertion and extraction reactions.

3.2. Particle fracture of LMO during reaction in the 4 V region

A charge–discharge cycle test for highly crystalline LMO was performed in the 4 V region to examine the particle fracture (Fig. 2 a). Following 100 cycles, the reversible capacity decreased from 125 mAh g⁻¹ to 85 mAh g⁻¹. According to the *ex-situ* XRD analysis of LMO electrodes (Fig. S2), the voltage plateaus at 4.5 V on charge and 3.3 V on discharge resulted from the formation and disappearance of a double hexagonal phase.⁶⁴ The SEM images of LMO particles following

the cycle test (Fig. 2 b, c) show that the extent of fracturing of the octahedral LMO particles during the cycle test was insignificant, because the dimensional change was approximately 3% in this region. Minute cracks parallel to the octahedral edges were observed, and there was no pulverization, indicating that highly crystalline LMO is very resistant to particle fracture. To accelerate particle fracture, LMO was examined under severe conditions, accelerated cycle tests, and overcharge tests.

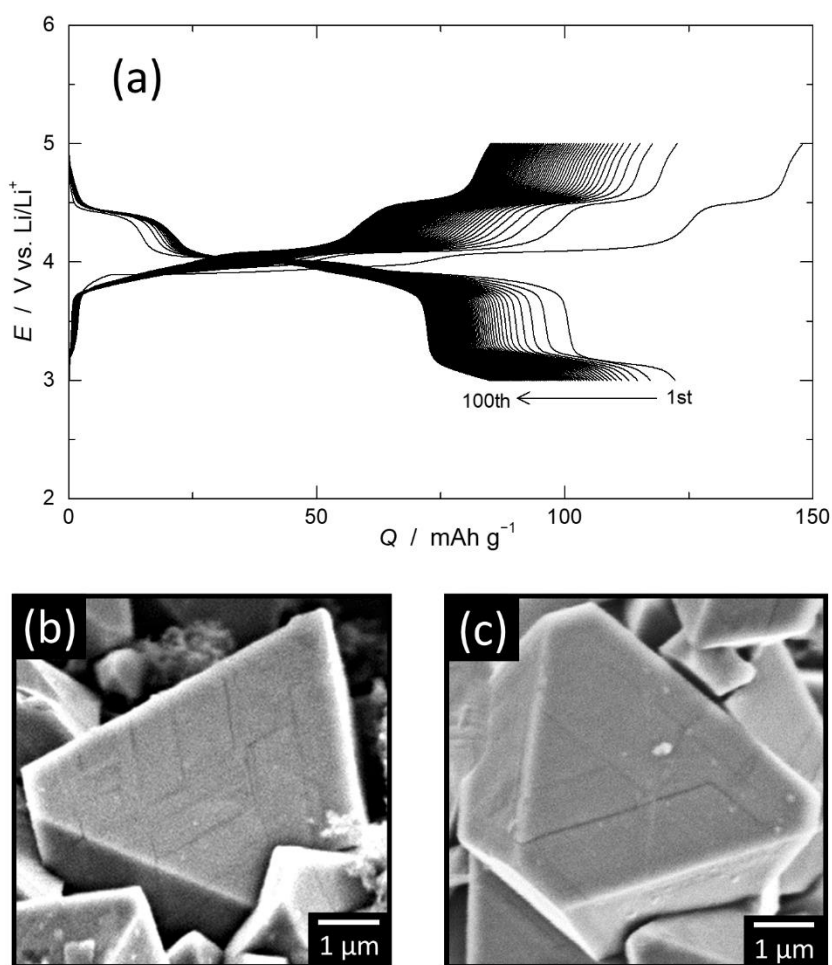


Figure 2. (a) Charge–discharge curves of a Li/LMO cell operated at a rate of 0.25 mA cm^{-2} at $25 \text{ }^\circ\text{C}$ for 100 cycles. The weight and thickness of the electrode-mixture are 53.2 mg and $112 \text{ }\mu\text{m}$ for LMO. (b, c) SEM images of LMO particles taken following the 100-cycle test.

An accelerated cycle test was performed, wherein an LTO/LMO cell was charged at a constant-voltage of 3.5 V (5.0 V vs. Li for LMO) for 6 min and discharged at 1.5 V (3.0 vs. Li for LMO) for 6 min (Fig. 3 a). The cell was cycled 2000 times. The current density decreased as the cycle number increased. The capacity at the 2000th cycle was approximately 47 mAh g^{-1} , corresponding to 32% of the theoretical capacity of 148 mAh g^{-1} . Since the charging and discharging rates are very high, a large concentration gradient of Li ions is developed in the particles. During the extraction of lithium from LMO, the lattice constant decreases as the Li ion concentration becomes low. Consequently, the internal stress should increase during the accelerated cycle test. Many small cracks were observed on the particle surface of LMO following 2000 cycles (Fig. 3 b), although no pulverization was noted. The cracks were parallel to the octahedral edges, indicating that the fracture planes were $\{111\}$ planes (Fig. 3 c). To investigate the effect of complex phase change of LMO in the 4 V region on the particle fracture, we performed the same accelerated test, which entailed a cubic single-phase reaction over the entire region, on $\text{Li}[\text{Li}_{0.1}\text{Mn}_{1.9}]\text{O}_4$.⁶⁴ The results depicted in Fig. S4 indicate that cracking parallel to the octahedral edges occurred and that the cracking pattern was identical to that of LMO. This implies that the observed cracking pattern is characteristic of materials having spinel structures undergoing a cubic single-phase reaction.

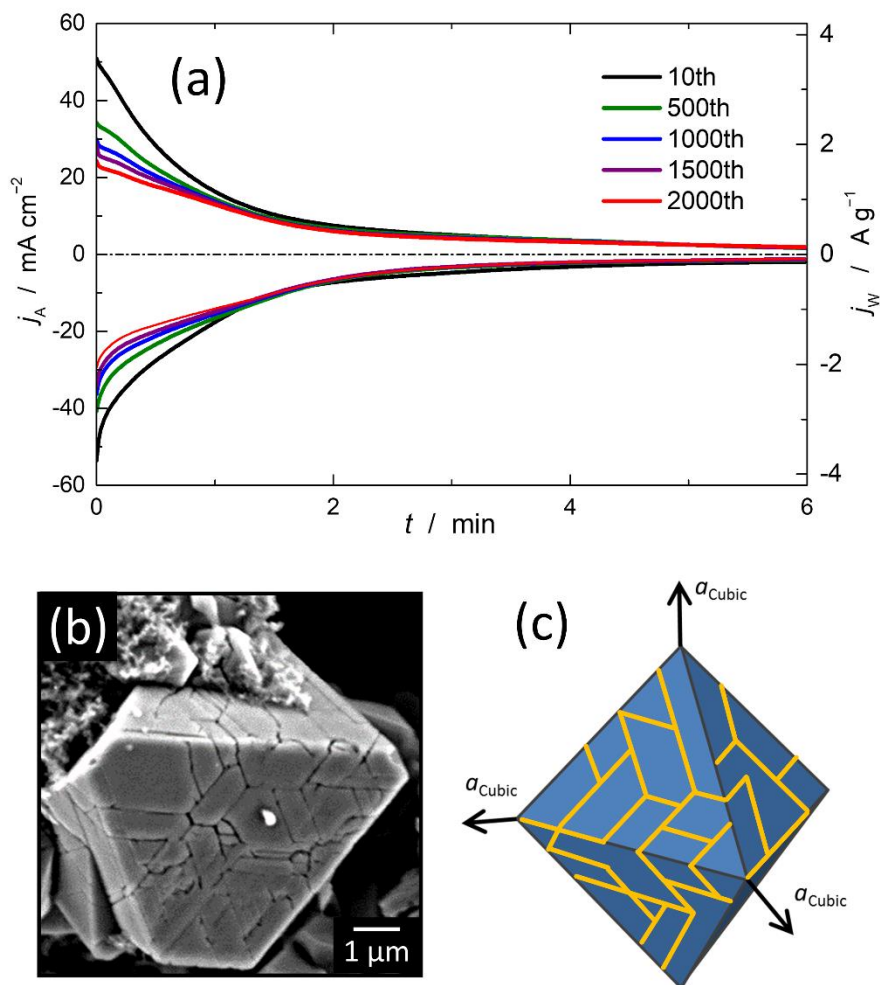


Figure 3. Charge-discharge curves of an LTO/LMO cell charged at a constant voltage of 3.5 V for 6 min and discharged at 1.5 V for 6 min. Current decays are shown for the 10th, 500th, 1000th, 1500th, and 2000th cycles. (b) SEM image of LMO particles taken following the accelerated cycle test. (c) Schematic of the crack pattern; yellow lines indicate cracks formed on the particle surface (blue).

There are two possible mechanisms for the particle fracture of LMO during cycling: fatigue cracking and stress corrosion cracking.^{66, 67} The former is derived from large cyclic strains, and the latter is derived from the combined influence of tensile stress and a corrosive environment. Because the LMO was charged at a high potential (5 V vs. Li) during the accelerated cycle test,

the acid generated by the decomposition of the electrolyte may affect the particle fracture. To determine whether the particle fracture of LMO is caused by fatigue cracking or stress corrosion cracking, an overcharge test of LMO was carried out (Fig. 4 a). In the overcharge test, the Li/LMO cell was charged at a constant current up to 6.0 V. Following the lithium extraction reaction at 4 V, the electrolyte was decomposed at voltages above 5 V. An excess capacity of $\sim 700 \text{ mAh g}^{-1}$ was observed until the cell voltage reached 6.0 V. Although the LMO electrode charged immediately, many heavy cracks were observed in the LMO particles following the overcharge test (Fig. 4 b). The octahedral shape was maintained. The fracture pattern was identical to that observed following the accelerated cycle test: the cracks were parallel to the octahedral edges. This result indicates that particle fracture during overcharging is related to electrolyte decomposition in the high-voltage region. During overcharging, the LMO particles were dissolved only at the cracks. If small cracks are present on the particle surface when it is exposed to an acid in the electrolyte, the cracks are propagated by stress corrosion cracking (Fig. 4 c). The constant-current cyclic testing results, in which LMO particles showed less cracking (Fig. 2), further demonstrates stress corrosion cracking occurring at high voltage. As the cell does not hold in the high voltage range ($> 4.8 \text{ V}$) during constant-current cyclic testing, only a small amount of HF is generated, resulting in no significant LMO-particle cracks. More remarkable cracks are expected to be observed after constant-current cycle testing if fracturing proceeded by the fatigue mechanism. Therefore, the fracture mechanism of LMO is deduced to be stress corrosion cracking instead of fatigue cracking. Stress corrosion cracking progresses during initial crack-formation and subsequent crack-growth processes. According to TEM observations of the crack-formation process at the atomic level, oxygen defects play an important role in crack nucleation.⁶⁸ In general, large particles contain more defects; therefore particle fracturing is more pronounced. However, LMO-particle fracturing

proceeds during stress corrosion cracking caused by the presence of HF in the 4 V region. Therefore, suppressing stress corrosion cracking on the surface is important for extending the cycle life of LMO; accordingly, large particles with small surface areas are appropriate. Furthermore, particles coated with substances resistant to HF can improve cyclability.⁶⁹⁻⁷¹

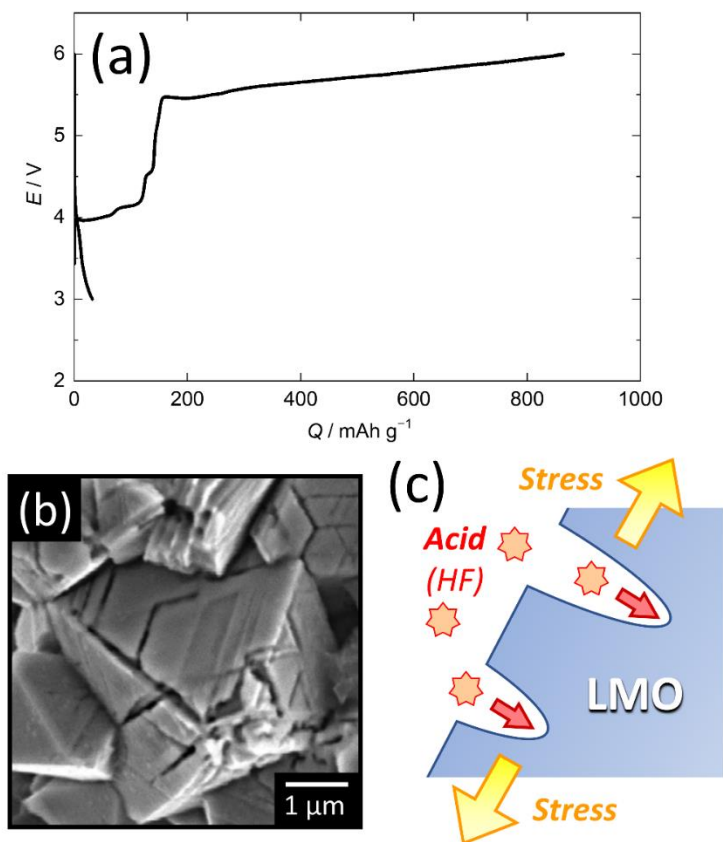


Figure 4. (a) Charge-discharge curves of an Li/LMO cell overcharged to 6.0 V at a rate of 0.25 mA cm⁻² at 25 °C. The weight and thickness of the LMO electrode were 108.7 mg and 233 μm, respectively. (b) SEM image of LMO particles taken following the overcharge test. (c) A schematic illustration of the stress corrosion cracking mechanism in which an acid generated by the decomposition of an electrolyte attacks the tips of cracks by dissolving the material.

3.3. Particle fracture of LMO during reaction in the 3 V region

To investigate particle fracture of the LMO during lithium insertion, wherein the cubic lattice is distorted to the tetragonal lattice, a Li/LMO cell was cycled at a rate of 0.25 mA cm^{-2} over a voltage ranges of 2.5–3.3 V at 25 °C (Fig. 5 a). The reversible capacity was $\sim 55 \text{ mAh g}^{-1}$, corresponding to 37% of the theoretical capacity. In this voltage region, the structural change of LMO is significant; the transformation between the cubic and tetragonal phases with 3% shrinkage along the a_T -axis and 12% elongation along the c_T -axis (Fig. S7). The anisotropic distortion of the crystal lattice induces a large dimensional mismatch at the grain boundary, resulting in particle fracture. Following 10 cycles, heavy cracks caused by intragranular fractures were observed in most particles (Fig. 5 b). The isolated LMO particle debris exfoliated by significant particle fracturing does not form electrical contacts. The loss of electron-conduction pathways has been reported to result in a capacity decrease associated with a rapid increase in polarization.⁷² Therefore, the capacity fading of LMO in the 3 V region is ascribable to the loss of electron-conduction pathways due to particle fracturing. Smaller particles containing fewer defects are expected to suppress particle fracturing in the 3 V region owing to the lower internal stress associated with dimensional mismatching. As shown in Fig. 5, two crack patterns were observed: one set of cracks was parallel to the edge, whereas the other was perpendicular to the edge (Fig. 5 c). The crack pattern observed in LMO operated in the 3 V region was different from that in the 4 V region, suggesting that the fracture mechanism is also different.

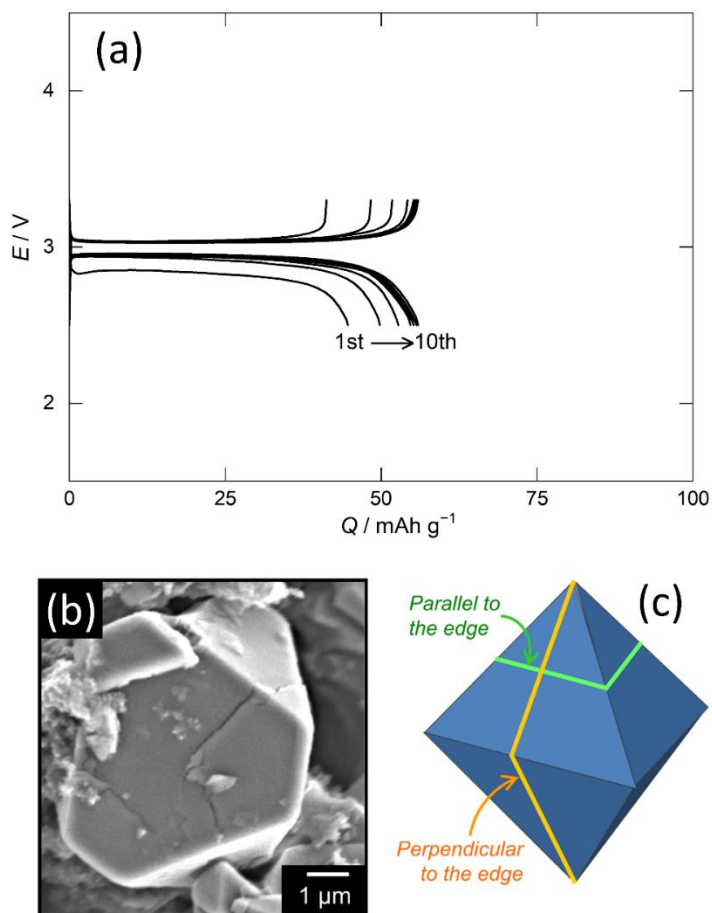


Figure 5. Charge and discharge curves of an Li/LMO cell operated at a rate of 0.25 mA cm^{-2} in the voltage range from 2.5 to 3.3 V at $25 \text{ }^\circ\text{C}$ for 10 cycles. (b) SEM image of LMO particles taken following the cycle test in the 3 V region. (c) A schematic illustration of the crack patterns; the cracks are formed parallel and perpendicular to the octahedral edges.

To reveal the fracture mechanism by monitoring the change in particle morphology, LMO was discharged to different extents, and the resulting LMO particles were observed using SEM (Fig. 6 a–c). As the lithium-insertion reaction proceeded, the octahedral particles were distorted by the bending of their edges. Cracks were small in the initial stage of the reaction, but were enlarged as the reaction proceeded. Since the initial LMO particles were single crystals having an octahedral shape with no grain boundaries, the particle shape is expected to change to a vertically stretched

octahedron that reflects the crystal system of the tetragonal lattice following the lithium-insertion reaction. However, the LMO particles in the fully discharged state were not shaped like a distorted octahedron, but instead like a three-dimensional star. This indicates that the LMO particles become polycrystalline following discharge, combining several tetragonal phases with different crystal orientations.

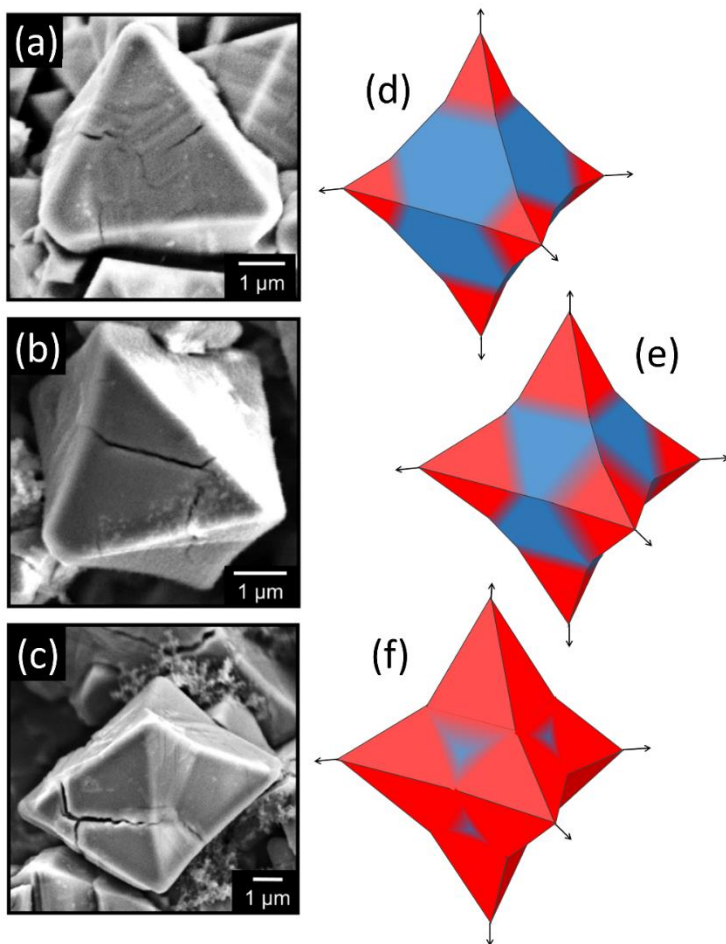


Figure 6. (a–c) SEM images of LMO particles discharged (Li insertion) to (a) 50, (b) 100, and (c) 140 mAh g⁻¹ of capacity. (d–f) Schematic of the structural transformation from cubic (blue) to tetragonal (red) phase. Tetragonal phases are nucleated at the vertex of the octahedron and expand into the particle.

The proposed mechanism for structural transformation from cubic to tetragonal phase to explain the particle shape change is illustrated in Fig. 6 d–f. When Li ions are inserted into octahedral LMO particles, tetragonal phases nucleate at the vertex of the octahedron. As the reaction proceeds, the grain boundaries between the cubic and tetragonal phases move toward the interior. At the end of discharge, the cubic phase disappears, and grain boundaries are formed between tetragonal phases. Overall, the octahedral single crystal of LMO particles in the initial state transforms into a three-dimensional star-shaped polycrystalline structure consisting of six tetragonal phases with different crystal orientations. We infer from the change in the particle shape that the cubic/tetragonal two-phase reaction proceeds via a nucleation-and-growth mechanism.

The two different crack patterns observed for discharged LMO particles (parallel and perpendicular to the octahedral edges) can be explained based on the change in particle shape (Fig. 7). In the initial stage of the lithium-insertion reaction, internal stresses are produced at the grain boundary between the cubic and tetragonal phases. In this case, cracks form along the [100] direction. The cubic/tetragonal grain boundary forms a plane perpendicular to the vertex, so that the fracture plane is the {100} plane (Fig. 7 c). In the deep discharge state, internal stress is produced at the grain boundary between two tetragonal phases. Consequently, the crack forms along the [110] direction, and the fracture plane is the {110} plane (Fig. 7 d). These results indicate that for intragranular fractures, the patterns of the cracks formed on the surfaces of lithium-insertion material particles are closely related to the internal stresses generated at the grain boundaries, where a large dimensional mismatch occurs.

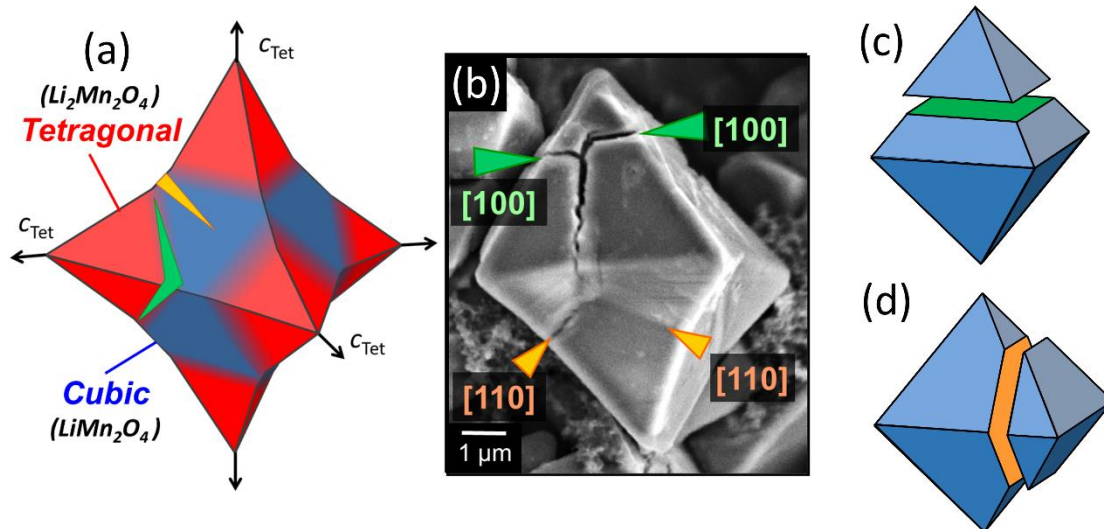


Figure 7. (a) Schematic illustration of crack formation at the grain boundaries of (green) cubic/tetragonal and (orange) tetragonal/tetragonal phases. (b) Two kinds of cracks formed on the surfaces of LMO particles. Fractures along (c) $\{100\}$ and (d) $\{110\}$ planes formed at the grain boundaries of cubic/tetragonal and tetragonal/tetragonal phases, respectively.

4. Conclusions

This study used highly crystalline single-crystal LMO spinel particles to infer the particle fracture mechanisms during lithium insertion/extraction reactions from the formation and propagation of cracks on the particle surface. In the reaction in the 4 V region of LMO where the isotropic dimensional change takes place, cracks occurred in the [111] direction parallel to the edges of the octahedral crystal, although the extent of fracture was unremarkable following 2000 charge–discharge cycles at a high rate. From the results of the overcharge test, the cracking progresses in the stress corrosion fracture mechanism involving the acid generated by the decomposition of the electrolyte. In the 3 V region, where LMO proceeds along a two-phase reaction pathway in which the crystal lattice changes anisotropically from a cubic to a tetragonal lattice, the tetragonal phase

nucleates at the vertex of the octahedron at the beginning, and the grain boundary of the cubic/tetragonal phases moves toward the interior of the crystal. Consequently, the octahedral LMO single crystal changes to a polycrystal having a star-shaped particle following lithium insertion. Furthermore, fracture due to internal stress occurs at the grain boundary with a large dimensional mismatch. The fracture planes are the $\{100\}$ planes at the cubic/tetragonal grain boundaries and the $\{110\}$ planes at the tetragonal/tetragonal grain boundaries. This study clarifies for the first time that the fracture mechanism of lithium-insertion materials differs depending on the reaction mechanism. To understand the fracture mechanism of lithium-insertion materials, it is necessary to consider various factors involved in the lithium insertion/extraction mechanism, particularly the structure of the grain boundary caused by the nucleation-and-growth mechanism, where the internal stress is significant because of the dimensional mismatch between the crystal lattices. Examining particle-fracturing phenomena from a macroscopic viewpoint provides a comprehensive understanding of fracture mechanisms that aid in the design of highly durable lithium-insertion materials when combined with atomic-level analyses.

Finally, we analyzed LMO particle sizes from the perspective of material improvement. Particle fracturing proceeds through the stress corrosion cracking mechanism in the high voltage region (above 4.5 V), although highly crystalline LMO particles exhibited no significant fracturing during cyclic testing in the 4 V region. This observation is indicative of a crucial problem for battery operation under severe conditions, such as float-charge and overcharge. Using LMO particles with small surface areas and smooth facets can suppress particle fracturing caused by stress corrosion cracking; this implies that highly crystalline materials likely exhibit better cyclability than nano-sized materials. In addition, large particles have lower contact resistances at the interfaces between the active materials and the current collector, which is a main component

of the resistance of a lithium insertion electrode.⁷³ Accordingly, we conclude that highly crystalline materials afford both improved cyclability and high power.

ASSOCIATED CONTENT

Supporting Information

The following files are available free of charge.

A one-figure-per-page document containing Figures S1–S6 (Microsoft Word, i.e., docx).

Schematic illustrations of internal stresses generated in lithium insertion materials; XRD patterns of LMO electrodes during charge and discharge; SEM images of LMO particles after the accelerated cycle test; Particle fracture of $\text{Li}[\text{Li}_{0.1}\text{Mn}_{1.9}]\text{O}_4$; SEM images of LMO particles after the overcharge test; SEM images of LMO particles after the cycle test in 3 V region; XRD patterns of LMO electrodes during discharge.

AUTHOR INFORMATION

Corresponding Author

Kingo Ariyoshi - Department of Applied Chemistry and Bioengineering, Graduate School of Engineering, Osaka City University, 3-3-138 Sugimoto, Sumiyoshi-ku, Osaka 558-8585, Japan.

Email: ariyoshi@osaka-cu.ac.jp

Author Contributions

The manuscript was written through contributions of all authors. All authors have given approval to the final version of the manuscript. K.A. developed the idea and wrote manuscript, N. U. prepared the materials, designed experiments.

ACKNOWLEDGMENT

We would like to thank Professor Emeritus Tsutomu Ohzuku of Osaka City University for his continuous encouragement on this research.

REFERENCES

- [1] Lu, L.; Han, X.; Li, J.; Hua, J.; Ouyang, M. A review on the key issues for lithium-ion battery management in electric vehicles. *J. Power Sources* **2013**, *226*, 272-288.
- [2] Hannan, M. A.; Hoque, M. M.; Mohamed, A.; Ayob, A. Review of energy storage systems for electric vehicle applications: Issues and challenges. *Renew. Sust. Energy Rev.* **2017**, *69*, 771-789.
- [3] Zeng, X.; Li, M.; Abd El-Hady, D.; Alshitari, W.; Al-Bogami, A. S.; Lu, J.; Amine, K. Commercialization of lithium battery technologies for electric vehicles. *Adv. Energy Mater.* **2019**, *9*, 1900161.
- [4] Barré, A.; Deguilhem, B.; Grolleau, S.; Gérard, M.; Suard, F.; Riu, D. A review on lithium-ion battery ageing mechanisms and estimations for automotive applications. *J. Power Sources* **2013**, *241*, 680-689.
- [5] Zhang, S.; Zhao, K.; Zhu, T.; Li, J. Electrochemomechanical degradation of high-capacity battery electrode materials. *Prog. Mater. Sci.* **2017**, *89*, 479-521.
- [6] Pender, J. P.; Jha, G.; Youn, D. H.; Ziegler, J. M.; Andoni, I.; Choi, E. J.; Heller, A.; Dunn, B. S.; Weiss, P. S.; Penner, R. M.; Mullins, C. B. Electrode degradation in lithium-ion batteries. *ACS Nano* **2020**, *14*, 1243-1295.
- [7] Ariyoshi, K.; Iwata, E.; Kuniyoshi, M.; Wakabayashi, H.; Ohzuku, T. Lithium aluminum manganese oxide having spinel-framework structure for long-life lithium-ion batteries. *Electrochem. Solid State Lett.* **2006**, *9*, A557.

- [8] Ariyoshi, K.; Yamato, R.; Makimura, Y.; Amazutsumi, T.; Maeda, Y.; Ohzuku, T. Three-volt lithium-ion battery consisting of $\text{Li}[\text{Ni}_{1/2}\text{Mn}_{3/2}]\text{O}_4$ and $\text{Li}[\text{Li}_{1/3}\text{Ti}_{5/3}]\text{O}_4$: improvement of positive-electrode material for long-life medium-power applications. *Electrochemistry* **2008**, *76*, 46-54.
- [9] Cabana, J.; Zheng, H.; Shukla, A. K.; Kim, C.; Battaglia, V. S.; Kunduraci, M. Comparison of the performance of $\text{LiNi}_{1/2}\text{Mn}_{3/2}\text{O}_4$ with different microstructures. *J. Electrochem. Soc.* **2011**, *158*, A997.
- [10] Ariyoshi, K.; Maeda, Y.; Kawai, T.; Ohzuku, T. Effect of Primary Particle Size upon Polarization and Cycling Stability of 5-V Lithium Insertion Material of $\text{Li}[\text{Ni}_{1/2}\text{Mn}_{3/2}]\text{O}_4$. *J. Electrochem. Soc.* **2011**, *158*, A281.
- [11] Mao, J.; Dai, K.; Zhai, Y. Electrochemical studies of spinel $\text{LiNi}_{0.5}\text{Mn}_{1.5}\text{O}_4$ cathodes with different particle morphologies. *Electrochim. Acta* **2012**, *63*, 381-390.
- [12] Ariyoshi, K.; Yamamoto, H.; Yamada, Y. High dimensional stability of LiCoMnO_4 as positive electrodes operating at high voltage for lithium-ion batteries with a long cycle life. *Electrochim. Acta* **2018**, *260*, 498-503.
- [13] Ariyoshi, K.; Eguchi, M.; Hirooka, M. Examining the long-term cyclabilities of $\text{Li}[\text{Ni}_{1/2}\text{Mn}_{3/2}]\text{O}_4$ and $\text{Li}[\text{Li}_{0.1}\text{Al}_{0.1}\text{Mn}_{1.8}]\text{O}_4$ using a full-cell configuration including LTO-counter electrodes with extra capacity. *J. Electrochem. Soc.* **2020**, *167*, 060532.
- [14] Bucci, G.; Swamy, T.; Chiang, Y. M.; Carter, W. C. Modeling of internal mechanical failure of all-solid-state batteries during electrochemical cycling, and implications for battery design. *J. Mater. Chem. A* **2017**, *5*, 19422-19430.

- [15] Tsai, P. C.; Wen, B.; Wolfman, M.; Choe, M. J.; Pan, M. S.; Su, L.; Thornton K.; Cabana, J.; Chiang, Y. M. Single-particle measurements of electrochemical kinetics in NMC and NCA cathodes for Li-ion batteries. *Energy Environ. Sci.* **2018**, *11*, 860-871.
- [16] Zhang, Y.; Zhao, C.; Guo, Z. Simulation of crack behavior of secondary particles in Li-ion battery electrodes during lithiation/de-lithiation cycles. *Int. J. Mech. Sci.* **2019**, *155*, 178-186.
- [17] Xu, R.; Yang, Y.; Yin, F.; Liu, P.; Cloetens, P.; Liu, Y.; Lin, F.; Zhao, K. Heterogeneous damage in Li-ion batteries: Experimental analysis and theoretical modeling. *J. Mech. Phys. Solids* **2019**, *129*, 160-183.
- [18] Christensen, J.; Newman, J. Stress generation and fracture in lithium insertion materials. *J. Solid State Electrochem.* **2006**, *10*, 293-319.
- [19] Christensen, J.; Newman, J. A mathematical model of stress generation and fracture in lithium manganese oxide. *J. Electrochem. Soc.* **2006**, *153*, A1019.
- [20] Woodford, W. H.; Chiang, Y. M.; Carter, W. C. "Electrochemical shock" of intercalation electrodes: a fracture mechanics analysis. *J. Electrochem. Soc.* **2010**, *157*, A1052.
- [21] Woodford, W. H.; Carter, W. C.; Chiang, Y. M. Strategies to avert electrochemical shock and their demonstration in spinels. *J. Electrochem. Soc.* **2014**, *161*, F3005.
- [22] Shin, Y.; Manthiram, A. Microstrain and capacity fade in spinel manganese oxides. *Electrochem. Solid State Lett.* **2002**, *5*, A55.

- [23] Hao, X.; Lin, X.; Lu, W.; Bartlett, B. M. Oxygen vacancies lead to loss of domain order, particle fracture, and rapid capacity fade in lithium manganospinel (LiMn_2O_4) batteries. *ACS Appl. Mater. Interfaces* **2014**, *6*, 10849-10857.
- [24] Watanabe, S.; Kinoshita, M.; Hosokawa, T.; Morigaki, K.; Nakura, K. Capacity fade of $\text{LiAl}_y\text{Ni}_{1-x-y}\text{Co}_x\text{O}_2$ cathode for lithium-ion batteries during accelerated calendar and cycle life tests (surface analysis of $\text{LiAl}_y\text{Ni}_{1-x-y}\text{Co}_x\text{O}_2$ cathode after cycle tests in restricted depth of discharge ranges). *J. Power Sources* **2014**, *258*, 210-217.
- [25] Ohzuku, T.; Tomura, H.; Sawai, K., Monitoring of particle fracture by acoustic emission during charge and discharge of Li/MnO_2 cells. *J. Electrochem. Soc.* **1997**, *144*, 3496.
- [26] Kalnaus, S.; Rhodes, K.; Daniel, C. A study of lithium ion intercalation induced fracture of silicon particles used as anode material in Li-ion battery. *J. Power Sources* **2011**, *196*, 8116-8124.
- [27] Tranchot, A.; Etienne, A.; Thivel, P. X.; Idrissi, H.; Roué, L. In-situ acoustic emission study of Si-based electrodes for Li-ion batteries. *J. Power Sources* **2015**, *279*, 259-266.
- [28] Rhodes, K.; Dudney, N.; Lara-Curzio, E.; Daniel, C. Understanding the degradation of silicon electrodes for lithium-ion batteries using acoustic emission. *J. Electrochem. Soc.* **2010**, *157*, A1354.
- [29] Winter, M.; Wrodnigg, G. H.; Besenhard, J. O.; Biberacher, W.; Novák, P. Dilatometric investigations of graphite electrodes in nonaqueous lithium battery electrolytes. *J. Electrochem. Soc.* **2000**, *147*, 2427.

- [30] Ohzuku, T.; Matoba, N.; Sawai, K. Direct evidence on anomalous expansion of graphite-negative electrodes on first charge by dilatometry. *J. Power Sources* **2001**, *97*, 73-77.
- [31] Nagayama, M.; Ariyoshi, K.; Yamamoto, Y.; Ohzuku, T. Characterization of lithium insertion electrodes by precision dilatometer: area-specific deformation of single electrode. *J. Electrochem. Soc.* **2014**, *161*, A1388.
- [32] Sauerteig, D.; Ivanov, S.; Reinshagen, H.; Bund, A. Reversible and irreversible dilation of lithium-ion battery electrodes investigated by in-situ dilatometry. *J. Power Sources* **2017**, *342*, 939-946.
- [33] Qi, Y.; Harris, S. J. In situ observation of strains during lithiation of a graphite electrode. *J. Electrochem. Soc.*, **2010**, *157*, A741.
- [34] Cannarella, J.; Arnold, C. B. State of health and charge measurements in lithium-ion batteries using mechanical stress. *J. Power Sources* **2014**, *269*, 7-14.
- [35] Mukhopadhyay, A.; Sheldon, B. W. Deformation and stress in electrode materials for Li-ion batteries. *Prog. Mater. Sci.* **2014**, *63*, 58-116.
- [36] Çapraz, Ö. Ö.; Rajput, S.; White, S.; Sottos, N. R. Strain evolution in lithium manganese oxide electrodes. *Exp. Mech.* **2018**, *58*, 561-571.
- [37] Wang, H.; Jang, Y. I.; Huang, B.; Sadoway, D. R.; Chiang, Y. M. TEM study of electrochemical cycling-induced damage and disorder in LiCoO₂ cathodes for rechargeable lithium batteries. *J. Electrochem. Soc.* **1999**, *146*, 473.

- [38] Dokko, K.; Nishizawa, M.; Horikoshi, S.; Itoh, T.; Mohamedi, M.; Uchida, I. In situ observation of LiNiO₂ single-particle fracture during Li-ion extraction and insertion. *Electrochem. Solid State Lett.* **2000**, *3*, 125.
- [39] Wang, D.; Wu, X.; Wang, Z.; Chen, L. Cracking causing cyclic instability of LiFePO₄ cathode material. *J. Power Sources* **2005**, *140*, 125-128.
- [40] Chao, S. C.; Yen, Y. C.; Song, Y. F.; Chen, Y. M.; Wu, H. C.; Wu, N. L. A study on the interior microstructures of working Sn particle electrode of Li-ion batteries by in situ X-ray transmission microscopy. *Electrochem. Commun.* **2010**, *12*, 234-237.
- [41] Lee, S. W.; McDowell, M. T.; Choi, J. W.; Cui, Y. Anomalous shape changes of silicon nanopillars by electrochemical lithiation. *Nano Lett.* **2011**, *11*, 3034-3039.
- [42] Liu, X. H.; Zheng, H.; Zhong, L.; Huang, S.; Karki, K.; Zhang, L. Q.; Liu, Y.; Kushima, A.; Liang, W. T.; Wang, J. W.; Cho, J.-H.; Epstein, E.; Dayeh, S. A.; Picraux, S. T.; Zhu, T.; Li, J.; Sullivan, J. P.; Cumings, J.; Wang, C.; Mao, S. X.; Ye, Z. Z.; Zhang, S.; Huang, J. Y. Anisotropic swelling and fracture of silicon nanowires during lithiation. *Nano Lett.* **2011**, *11*, 3312-3318.
- [43] Ryu, I.; Choi, J. W.; Cui, Y.; Nix, W. D. Size-dependent fracture of Si nanowire battery anodes. *J. Mech. Phys. Solids* **2011**, *59*, 1717-1730.
- [44] Liu, X. H.; Zhong, L.; Huang, S.; Mao, S. X.; Zhu, T.; Huang, J. Y. Size-dependent fracture of silicon nanoparticles during lithiation. *ACS Nano* **2012**, *6*, 1522-1531.

- [45] Yan, P.; Zheng, J.; Gu, M.; Xiao, J.; Zhang, J. G.; Wang, C. M. Intragranular cracking as a critical barrier for high-voltage usage of layer-structured cathode for lithium-ion batteries. *Nat. Commun.* **2017**, *8*, 1-9.
- [46] Lim, J. M.; Hwang, T.; Kim, D.; Park, M. S.; Cho, K.; Cho, M. Intrinsic origins of crack generation in Ni-rich $\text{LiNi}_{0.8}\text{Co}_{0.1}\text{Mn}_{0.1}\text{O}_2$ layered oxide cathode material. *Sci. Rep.* **2017**, *7*, 1-10.
- [47] Qian, G.; Zhang, Y.; Li, L.; Zhang, R.; Xu, J.; Cheng, Z.; Xie, S.; Wang, H.; Rao, Q.; He, Y.; Shen, Y.; Chen, L.; Tang, M.; Ma, Z. F. Single-crystal nickel-rich layered-oxide battery cathode materials: synthesis, electrochemistry, and intra-granular fracture. *Energy Storage Mater.* **2020**, *27*, 140-149.
- [48] Lin, Q.; Guan, W.; Zhou, J.; Meng, J.; Huang, W.; Chen, T.; Gao, Q.; Wei, X.; Zeng, Y.; Zhang, Z. Ni-Li anti-site defect induced intragranular cracking in Ni-rich layer-structured cathode. *Nano Energy* **2020**, *76*, 105021.
- [49] Zhao, K.; Pharr, M.; Vlassak, J. J.; Suo, Z. Fracture of electrodes in lithium-ion batteries caused by fast charging. *J. Appl. Phys.* **2010**, *108*, 073517.
- [50] Hu, Y.; Zhao, X.; Zhigang, S. Averting cracks caused by insertion reaction in lithium-ion batteries. *J. Mater. Res.* **2010**, *25*, 1007-1010.
- [51] Cheng, Y. T.; Verbrugge, M. W. Evolution of stress within a spherical insertion electrode particle under potentiostatic and galvanostatic operation. *J. Power Sources* **2009**, *190*, 453-460.

- [52] Verbrugge, M. W.; Cheng, Y. T. Stress and strain-energy distributions within diffusion-controlled insertion-electrode particles subjected to periodic potential excitations. *J. Electrochem. Soc.* **2009**, *156*, A927.
- [53] Zhu, M.; Park, J.; Sastry, A. M. Fracture analysis of the cathode in Li-ion batteries: A simulation study. *J. Electrochem. Soc.* **2012**, *159*, A492.
- [54] Zhang, X.; Shyy, W.; Sastry, A. M. Numerical simulation of intercalation-induced stress in Li-ion battery electrode particles. *J. Electrochem. Soc.* **2007**, *154*, A910.
- [55] Park, J.; Lu, W.; Sastry, A. M. Numerical simulation of stress evolution in lithium manganese dioxide particles due to coupled phase transition and intercalation. *J. Electrochem. Soc.* **2010**, *158*, A201.
- [56] Qi, Y.; Xu, Q.; Van der Ven, A. Chemically induced crack instability when electrodes fracture. *J. Electrochem. Soc.* **2012**, *159*, A1838.
- [57] Grantab, R.; Shenoy, V. B. Location-and orientation-dependent progressive crack propagation in cylindrical graphite electrode particles. *J. Electrochem. Soc.* **2011**, *158*, A948.
- [58] Yang, B.; He, Y. P.; Irsa, J.; Lundgren, C. A.; Ratchford, J. B.; Zhao, Y. P. Effects of composition-dependent modulus, finite concentration and boundary constraint on Li-ion diffusion and stresses in a bilayer Cu-coated Si nano-anode. *J. Power Sources* **2012**, *204*, 168-176.
- [59] Gao, Y. F.; Zhou, M. Coupled mechano-diffusional driving forces for fracture in electrode materials. *J. Power Sources* **2013**, *230*, 176-193.

- [60] Huang, S.; Fan, F.; Li, J.; Zhang, S.; Zhu, T. Stress generation during lithiation of high-capacity electrode particles in lithium ion batteries. *Acta Mater.* **2013**, *61*, 4354-4364.
- [61] Brassart, L.; Zhao, K.; Suo, Z. Cyclic plasticity and shakedown in high-capacity electrodes of lithium-ion batteries. *Int. J. Solids and Struct.* **2013**, *50*, 1120-1129.
- [62] Ohzuku, T.; Kitagawa, M.; Hirai, T. Electrochemistry of manganese dioxide in lithium nonaqueous cell: III. X-Ray diffractational study on the reduction of spinel-related manganese dioxide. *J. Electrochem. Soc.* **1990**, *137*, 769.
- [63] Ariyoshi, K.; Yamato, R.; Ohzuku, T. Zero-strain insertion mechanism of $\text{Li}[\text{Li}_{1/3}\text{Ti}_{5/3}]\text{O}_4$ for advanced lithium-ion (shuttlecock) batteries. *Electrochim. Acta* **2005**, *51*, 1125-1129.
- [64] Palacin, M. R.; Chabre, Y.; Dupont, L.; Hervieu, M.; Strobel, P.; Rousse, G.; Masquelier, C.; Anne, M.; Amatucci, G. G.; Tarascon, J. M. On the origin of the 3.3 and 4.5 V steps observed in LiMn_2O_4 -based spinels. *J. Electrochem. Soc.* **2000**, *147*, 845.
- [64] Imazaki, M.; Ariyoshi, K.; Ohzuku, T. An approach to 12 V “lead-free” batteries: Tolerance toward overcharge of 2.5 V battery consisting of LTO and LAMO. *J. Electrochem. Soc.* **2009**, *156*, A780-A786.
- [66] Wachtman, J.; Cannon, W.; Matthewson, M. *Mechanical properties of ceramics*, 2nd ed.; John Wiley & Sons, 2009.
- [67] Janssen, M. *Fracture mechanics*, 2nd ed.; Spon Press, 2004.

- [68] Lee, S.; Jin, W.; Kim, S. H.; Joo, S. H.; Nam, G.; Oh, P.; Kim, Y.-K.; Kwak, S. K.; Cho, J. Oxygen vacancy diffusion and condensation in lithium-ion battery cathode materials. *Angew. Chem.* **2019**, *131*, 10588-10595.
- [69] Arrebola, J. C.; Caballero, A.; Hernán, L.; Morales, J. Re-examining the effect of ZnO on nanosized 5V $\text{LiNi}_{0.5}\text{Mn}_{1.5}\text{O}_4$ spinel: An effective procedure for enhancing its rate capability at room and high temperatures. *J. Power Sources* **2010**, *195*, 4278-4284.
- [70] Pang, W. K.; Lin, H.-F.; Peterson, V. K.; Lu, C.-Z.; Liu, C.-E.; Liao, S.-C.; Chen, J.-M. Enhanced rate-capability and cycling-stability of 5 V SiO_2 - and polyimide-coated cation ordered $\text{LiNi}_{0.5}\text{Mn}_{1.5}\text{O}_4$ lithium-ion battery positive electrodes. *J. Phys. Chem. C* **2017**, *121*, 3680-3689.
- [71] Wang, A.-M.; Bai, N. Improved electrochemical cycling performance of high-voltage spinel $\text{LiNi}_{0.5}\text{Mn}_{1.5}\text{O}_4$ cathode materials by coating with spinel MgAl_2O_4 . *Solid State Ionics* **2019**, *336*, 19-25.
- [72] Ariyoshi, K.; Ino, I.; Yamada, Y.; Rate capability of carbon-free lithium titanium oxide electrodes related to formation of electronic conduction paths observed by color change. *J. Power Sources* **2019**, *430*, 150-156.
- [73] Ariyoshi, K.; Tanimoto, M.; Yamada, Y.; Impact of particle size of lithium manganese oxide on charge transfer resistance and contact resistance evaluated by electrochemical impedance analysis. *Electrochim. Acta* **2020**, *364*, 137292

Table of Contents

